T Markovic et al.

# Measurements and modelling of plasma response field to RMP on the COMPASS tokamak

# Measurements and modelling of plasma response field to RMP on the COMPASS tokamak

**T. Markovic**[1,2]**, Y. Q. Liu**[3]**, P. Cahyna**[1]**, R. Pánek**[1]**, M. Peterka**[1,2]**, M. Aftanas**[1]**, P. Bílková**[1]**, P. Bohm**[1]**, M. Imríšek**[1,2]**, P. Háček**[1]**, J. Havlicek**[1]**, A. Havránek**[1,4]**, M. Komm**[1]**, J. Urban**[1]**, the COMPASS Team**[1]

[1] Institute of Plasma Physics CAS, Za Slovankou 1782/3, 180 00, Prague, Czech Republic
[2] Charles University in Prague, Faculty of Mathematics and Physics, Ke Karlovu 3, 121 00, Prague, Czech Republic
[3] CCFE, Culham Science Centre, Abingdon, OX14 3DB, United Kingdom
[4] Czech Technical University in Prague, Faculty of Electrical Engineering, Technická 2, 166 27, Prague, Czech Republic

E-mail: `markovic@ipp.cas.cz`

**Abstract.** It has been shown on several tokamaks that application of a Resonant Magnetic Perturbation (RMP) field on plasma can under certain conditions lead to suppression or mitigation of Edge-Localized Mode (ELM) instabilities. Due to the rotation of the plasma in the RMP field reference system, currents are induced on resonant surfaces within the plasma, consequently, screening the original perturbation. In this work, the extensive set of 104 saddle loops installed on the COMPASS tokamak [1] is utilized to measure the plasma response field for two $n = 2$ RMP configurations of different $m$ spectrum. It is shown that spatially the response field is in anti-phase to the original perturbation, and that the poloidal profile of the measured response field does not depend on the $m$ profile of used RMP. Simulations of the plasma response by linear MHD code MARS-F [2] reveal that both studied RMP configurations are well screened by the plasma. Comparison of measured plasma response field to the simulated one shows a good agreement across the majority of $\theta$ angle, with exception of $\theta \approx 0$ low-field side area, where discrepancy is seen.

## 1. Introduction

During the tokamak operation in high energy confinement mode (H-mode), plasma experiences periodic relaxation of its edge gradient in pedestal region which are known as Edge-Localized Modes (ELMs), that carry the energy of bulk plasma to the tokamak wall. The unmitigated type I ELMs are a major concern for the operation of the ITER device, since the energy they carry is sufficient to damage the first wall and the plasma divertor [3]. Recent work [4] offers a comprehensive review of investigated Type I ELM mitigation techniques, namely high-velocity injection of frozen Deuterium pellets into the plasma [5], fast movement of plasma position [6] and the non-axisymmetric perturbation of plasma equilibrium by radial field generated by Resonant Magnetic Perturbation (RMP) coils [7].

The successful Type I ELM mitigation or suppression by RMP has already been demonstrated on number of devices [8, 9, 10, 11]. However, the exact physical mechanism of the mitigation is not yet fully understood and thus, the extensive dedicated experimental effort is supported by a modelling of the RMP effects on plasma with a variety of numerical codes (reviewed in [12]). One of the leading theories of plasma response to the RMP (supported by recent observations in [13]) states that when the hot conducting plasma is rotating in the reference frame connected with the RMP field, the screening currents are generated on corresponding resonant magnetic surfaces.

This work compares the experimental observations of the RMP plasma response on the COMPASS tokamak to the model based on the theory above. This paper is organized as follows: Section 2 introduces the COMPASS system for RMP field generation as well as the magnetic diagnostics used to measure the plasma response to the RMP. Subsequently, Section 3 provides the measured plasma RMP response for two studied RMP field configurations. In Section 4 the results of the modelling of plasma RMP response by a linear MHD code MARS-F [2] are presented. The spectra of generated perturbations mapped for the respective plasma equilibria are shown and the effect of plasma is discussed. In the last part of the paper in Section 5, the measured and the modelled plasma responses are compared to each other, with similarities and differences discussed. The work is then summarized, with future work outlined, in Section 6.

## 2. Experimental arrangement

### 2.1. RMP field generation in the COMPASS tokamak

The tokamak COMPASS is a compact-sized ($R = 0.56$ m, $a = 0.2$ m) experimental device of ITER-like cross section, operated in diverted plasma regime [1] (for more information about discharge parameters used in this work, see Section 4.2). Its RMP coil system consists of series of independent ex-vessel conductors, that cover the whole vacuum chamber and can be connected into a variable saddle coil configuration [14]. This offers a unique variability of the poloidal mode number $m$ spectrum of the generated
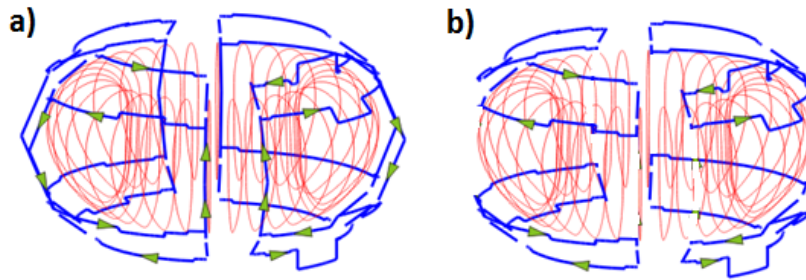
**Figure 1.** COMPASS RMP coil configurations used in this study. a) *On+off-midplane RMP configuration.* b) *Off-midplane RMP configuration.* Blue lines represent RMP windings, green arrows show direction of current, red lines represent plasma separatrix.

RMP. The two specific RMP configurations investigated in this work are depicted in Fig. 1a) and b) and are referred as *on+off-midplane* configuration and *off-midplane* configuration, respectively. All the coils are single-turned, off-midplane coils being of even parity while the midplane coil of opposite polarity to them. Toroidally, the windings cover tokamak quadrants, generating RMP field with toroidal mode number $n = 1, 2$. In this work, the $n = 2$ field is used, since $n = 1$ field is more prone to causing mode locking of magnetic islands that are typically present in the plasma [14].

The RMP power supplies enable a single DC pulse per tokamak discharge of the same current magnitude in all of the RMP coils. The temporal evolution of the current waveform has the form of trapezoid, with flat-top phase lasting several tens of ms and current ramps from units to tens of ms. The arrangement of the conductors generating the RMP uses two independent GBT power supplies based on the design described in [15], but capable of producing higher voltage. This, however, limits the possible field configurations currently.

### 2.2. Magnetic diagnostics of the RMP field

The tokamak chamber is covered by a set of 104 ex-vessel saddle loops, arranged into 4 quadrants (radially located below the RMP coil quadrants), as depicted in Fig. 2. Poloidal and toroidal angles ($\theta$ and $\phi$, respectively) are shown for reference.

Each of the 4 quadrant sets consists of 22 large saddle loops covering the whole quadrant in toroidal direction (e.g. SE1-22), and of 4 smaller saddle loops on Low-Field Side (LFS), that cover both octants per quadrant in two poloidal rows (e.g. SSE1-2 and ESE1-2). In order to cover the whole chamber, it is necessary for the loops to often adopt a more complex shape to avoid vacuum vessel ports. Moreover, simplified scheme in Fig. 2 does not take into account that the loops cover different poloidal range, as seen from the in-scale Fig. 3. Note, however, that the loop geometry was taken into consideration in the evaluation of the magnetic field signals presented in this work.

The poloidal cut of the COMPASS tokamak in Fig. 3 depicts the relative positions of tokamak chamber, diagnostic saddle loops, RMP coils and typical plasma separatrix.
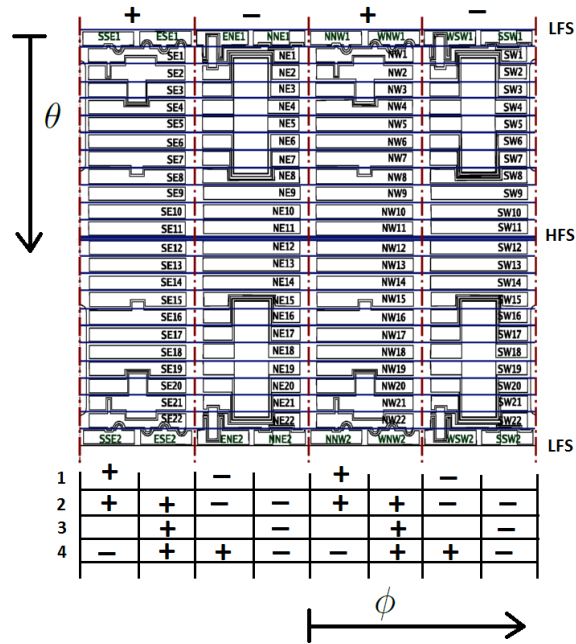
**Figure 2.** Scheme (not in scale) of 104 diagnostic saddle loops covering the chamber. Poloidal and toroidal angles $\theta$ and $\phi$, respectively are shown, as well as Low-Field Side *LFS* and High-Field Side *HFS* poloidal positions. Signs in the rows represent possible combinations of loop signals in order to obtain $n = 2$ component, with the row in the top corresponding to large quadrant loops and 4 bottom rows corresponding to octant loops.
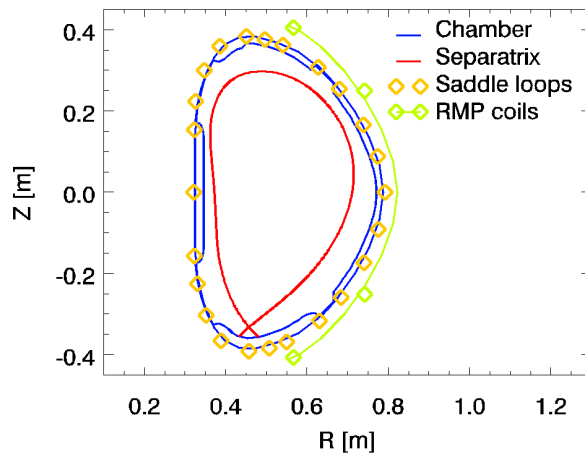


**Figure 3.** Poloidal cut of the COMPASS tokamak showing positions of separatrix (red line), tokamak chamber (blue lines), diagnostic saddle loop ends (orange symbols) and RMP windings (green line and symbols). Note that each saddle loop and RMP coil cover the whole poloidal surface between 2 corresponding symbols.

This illustrates that on the COMPASS tokamak:

- Plasma separatrix is located close to RMP coils.
- The RMP coils cover large poloidal sections, especially the coil on midplane.

- Diagnostic saddle loops are of different size, with the largest area loops located on *High Field Side* (HFS) and the smallest area loops located on the top and the bottom part of chamber.

- There is sufficient number of saddle loops located underneath the RMP coils to provide good information about the spatial distribution of the RMP field.

By an appropriate combination of the signals of each poloidal row of the saddle loops across all the 4 toroidal quadrants as illustrated by the signs in Fig. 2, namely:

$$B_{n2} = \frac{1}{4} \left( B_n^{NW} - B_n^{SW} + B_n^{SE} - B_n^{NE} \right), \tag{1}$$

a quantity of $B_{n2}$ is obtained. This represents the $n = 2$ harmonic part of the normal component of the magnetic field. It should be noted, that the quantity is averaged not only across the toroidal quadrant, but also across the poloidal span of the chosen row of saddle loops. Given the unique diagnostic arrangement on the COMPASS tokamak, it is possible to measure $B_{n2}$ on up to 22 different poloidal positions. Moreover, with the two rows of small octant-covering saddle loops on LFS, there are 4 possible combinations of obtaining the $B_{n2}$ quantity (as shown in the bottom part of Fig. 2), therefore, measurements on 4 different toroidal positions $\phi$ (corresponding to the center of used octant or quadrant) are provided. Note, that combination No. 2 is equivalent to those of the large quadrant loops. As the loops are located outside of the vessel, the high-frequency part of $B_{n2}$ is cut-off by skin effect at the frequency of approximately 40 kHz. However, this is of no concern since only the flat-top part of the DC RMP pulse is analyzed in this paper. The RMP current driven by the two independent power supplies is measured with a set of two Rogowski coils.

## 3. Measurement of plasma response to RMP field

| Discharge number | 8078 | 9655 |
|:---:|:---:|:---:|
| RMP configuration | *On+off-midplane* | *Off-midplane* |
| $B_\phi$ [T] | 1.14 | 1.14 |
| $I_{\text{plasma}}$ [kA] | 230 | 230 |
| $<n_e>$ [$10^{19}\text{m}^{-3}$] | 6.5 | 6.0 |
| $q_{95}$ [-] | 3.6 | 3.5 |
| $I_{\text{RMP}}$ [kA] | 1.5 | 1.8 |

**Table 1.** Parameters of the analyzed discharges.

To study the plasma response to the RMP field on COMPASS, two similar discharges with different RMP configurations were chosen. Namely, discharge #8078, with on+off-midplane RMP configuration, and discharge #9655, with off-midplane RMP configuration are considered and compared. The summary of their basic parameters is presented in Tab. 1, with $B_\phi$ representing the toroidal magnetic field, $I_{\text{plasma}}$ the
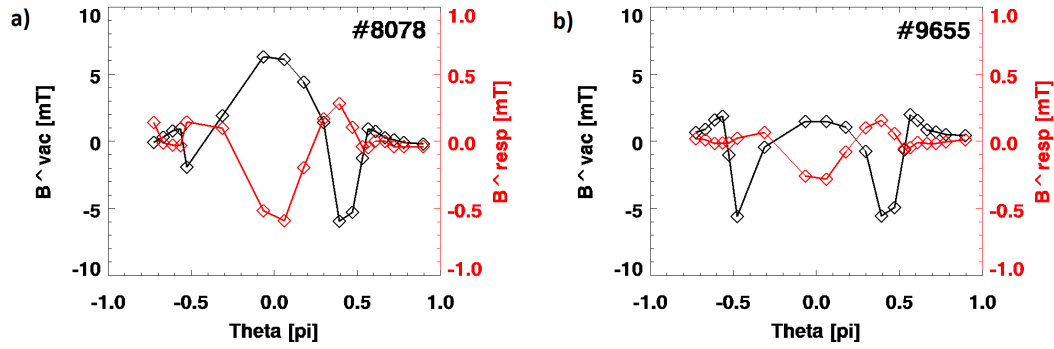
**Figure 4.** Full poloidal angle $\theta$ profile of measured $B_{n2}^{Vac}$ (black) and $B_{n2}^{Resp}$ (red) components. a) Discharge #8078 of on+off-midplane RMP. b) Discharge #9655 of off-midplane RMP. Note that the absence of RMP field peak at $\theta = -0.5 \cdot \pi$ in Fig. a) is due to malfunction of detection loop.
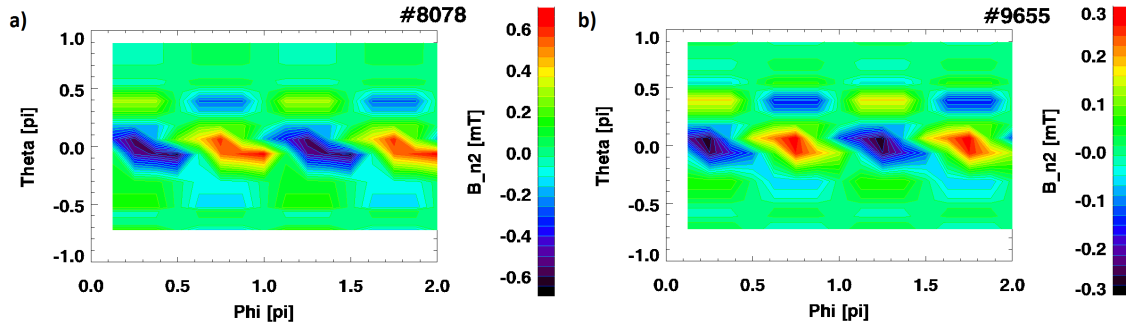


**Figure 5.** Full $\theta - \phi$ profile of $B_{n2}^{Resp}$ measured by the saddle loops. a) On+off-midplane configuration of discharge #8078. b) Off-midplane configuration of discharge #9655. $\theta$ profiles in Fig. 4 correspond to $\phi = 0.25 \cdot \pi$ position.

plasma current, $<n_e>$ the line-averaged electron density, $q_{95}$ the safety factor and $I_{\mathrm{RMP}}$ then current in RMP coils. Further information on profiles of the electron and ion temperatures and density are provided in Fig. 7 and discussed in Section 4.2.

Due to its electro-magnetic nature, the plasma screening effect on the spectrum of generated RMP (see Section 4 for details) can be detected by the magnetic diagnostic system of the saddle loops. During the RMP waveform, the measured $B_{n2}$ quantity from eq. (1) is equivalent to

$$B_{n2}^{Tot}(\theta_j) = B_{n2}^{Vac}(\theta_j) + B_{n2}^{Resp}(\theta_j). \tag{2}$$

There, the original perturbation $B_{n2}^{Vac}$ was altered by the plasma response field $B_{n2}^{Resp}$. Taking into account the total mutual inductance $M(\theta_j)$ between RMP coils and the corresponding saddle loop combination of poloidal position $\theta_j$ (measured by performing a vacuum shot with the RMP pulse of given coil configuration), the original perturbation signal is obtained from:

$$B_{n2}^{Vac}(\theta_j) = \frac{M(\theta_j)}{S(\theta_j)} \cdot I_{\mathrm{RMP}}. \tag{3}$$

$S(\theta_j)$ represents the total effective surface of the saddle loop row $j$ and $I_{\mathrm{RMP}}$ represents current in the RMP coils.

The resulting poloidal profile of the plasma response field $B_{n2}^{Resp}$, as well as that of the original perturbation $B_{n2}^{Vac}$, is shown in Fig. 4a) and b) for on+off-midplane and off-midplane RMP configuration respectively. In both cases, the $B_{n2}^{Resp}$ is close to being in anti-phase to the $B_{n2}^{Vac}$, implying that screening of the perturbation is dominant over its penetration into plasma. Interestingly, the strongest plasma response is observed in the LFS area of $\theta \approx 0$, regardless of the RMP field configuration used. Specifically, in both configurations the ratio of $B_{n2}^{Resp}$ under the bottom/top row RMP coils to the $B_{n2}^{Resp}$ on midplane is approximately the same ($\approx 0.5$). This implies that the midplane RMP coil row on COMPASS primarily affects the amplitude of the response, however, not its poloidal profile. It is also observed that $B_{n2}^{Resp}$ is approximately by an order smaller than $B_{n2}^{Vac}$, which is further discussed in Section 5.

Sketched coil combinations in Fig. 2 show that $B_{n2}$ combinations are identical with respect to $\Delta\phi = \pi$ shift and only opposite in polarity with respect to $\Delta\phi = \pi/2$ shift. Therefore, the $\theta - \phi$ distribution of the $B_{n2}^{Resp}$ can be illustrated by assigning the measured $B_{n2}^{Resp}$ values to the whole quadrant and, afterwards, extended to the whole $\phi$ by using the symmetry described above. Moreover, the octant-covering saddles on LFS offer $B_{n2}^{Resp}$ measurements on 4 different $\phi$ locations per quadrant. Thanks to the good spatial resolution of octant saddles, it can be seen from $B_{n2}^{Resp}$ $\theta - \phi$ plot in Fig. 5 that the plasma response field to both RMP configurations is in fact of helical nature, rather than being strictly in anti-phase to the imposed RMP field. This helical character is also further discussed in Section 5, with respect to the modeling.

## 4. Modelling of plasma response

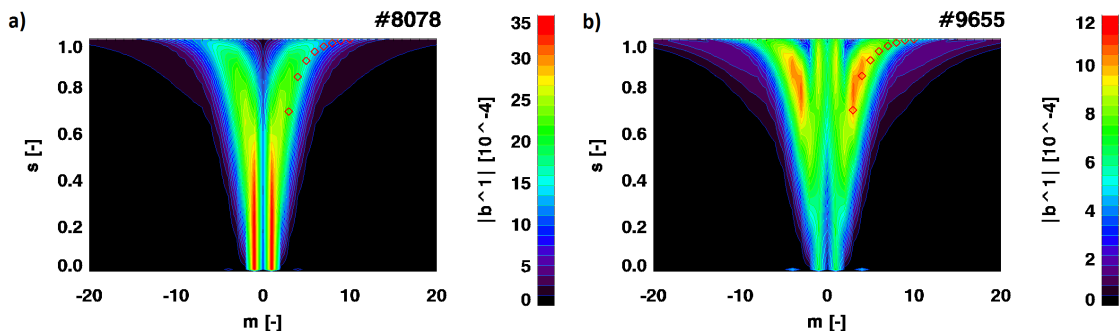### 4.1. MARS-F code and modelled perturbation



**Figure 6.** Spectrograms of the $n = 2$ vacuum RMP field $|b_{mn}^1|$, calculated by MARS-F code. a) On+off-midplane configuration of discharge #8078. b) Off-midplane configuration of discharge #9655. Red symbols represent positions where condition $q = m/n$ is fulfilled.

The plasma response to both RMP configurations was modelled using the linear

resistive MHD code MARS-F [2]. This code solves the linearized single-fluid MHD equations, assuming that resulted perturbation of plasma equilibrium remains small [16]. Essentially, the non-axisymmetric RMP perturbation is imposed on the axisymmetric plasma equilibrium and a forced eigenvalue problem of stability is solved [12].

The unperturbed magnetic equilibrium of both discharges is provided by numerical code EFIT++ [17, 18], with the local magnetic measurements, the total plasma current $I_{\text{plasma}}$ and the toroidal magnetic field $B_\phi$ used as an input. In both cases, the chosen equilibrium corresponds to the time moment of 1164 ms, i.e. to the flat-top phase of the RMP current waveform. In addition, the cross-talk of the RMP field on the magnetic measurements used as the input for the equilibrium reconstruction was eliminated in the same manner as shown in Eq. (3). The magnetic equilibria were remapped to straight fieldline coordinate system, using the equilibrium solver CHEASE [19], prior to be used as the input for the MARS-F code. However, since the code requires a finite, well-defined $q(a)$, the plasma X-point was slightly smoothed in the process of re-mapping.

The RMP coils are represented as toroidally aligned straight lines of finite poloidal width, that carry a toroidal harmonic current $\sim \exp{(in\phi)}$ (with $n = 2$ in this paper) [20]. This representation naturally differs from the real coil geometry, and thus the RMP field calculated by MARS-F was compared to the RMP field calculation by the Biot-Savart's law based ERGOS code [21, 22], which takes into account the real coil geometry. A good agreement in the RMP field components aligned with the pitch angle of the magnetic equilibrium was observed between the both codes and the coil representation was considered satisfactory.

The relevant quantity, that contains the information on the spectrum of the RMP field used in this paper, is represented by a normal field component [21]:

$$|b_{mn}^1| = \left| \frac{2}{R_0^2 B_0} \frac{1}{\mathrm{d}\psi_p/\mathrm{d}s} \frac{\mathbf{b} \cdot \nabla\psi}{\mathbf{B_{eq}} \cdot \nabla\phi} \right|. \tag{4}$$

Note that $|b_{mn}^1|$ above corresponds to the definition used in the ERGOS code. While the $n = 2$ is fixed for the applied perturbation field, there are many poloidal mode number $m$ harmonics, whose distribution is also radially dependent. The spectra of the two studied RMP configurations (for the given plasma equilibria) are shown in Fig. 6. $s = \sqrt{\psi_p}$ and $\psi_p = \frac{\psi - \psi_0}{\psi_a - \psi_0}$, with the poloidal magnetic flux $\psi$ being normalized with respect to the magnetic axis flux $\psi_0$ and to the magnetic flux on the plasma separatrix $\psi_a$. Note, that $s \approx r/a$.

Figure 6 shows the vacuum RMP field, i.e. without the effect of plasma, for reference. Comparison of Fig. 6a) to Fig. 6b), implies that the absence of large midplane row RMP coils has a significant effect on the amplitude of the field, which is approximately half as strong in magnitude if this row is absent. Distribution-wise, this leads to the shift of the pronounced $m \pm 1$ harmonics from the plasma center to the edge regions, leading to much weaker magnitude of the generated RMP field on the midplane (see vacuum field in Fig. 4). The red symbols show the location of the resonant surfaces with the condition $q = \frac{m}{n=2}$ fulfilled. Having them located close to

the ridge of the spectrum, rather than its valleys implies good resonance between the plasma equilibrium and the vacuum RMP field on the COMPASS tokamak.
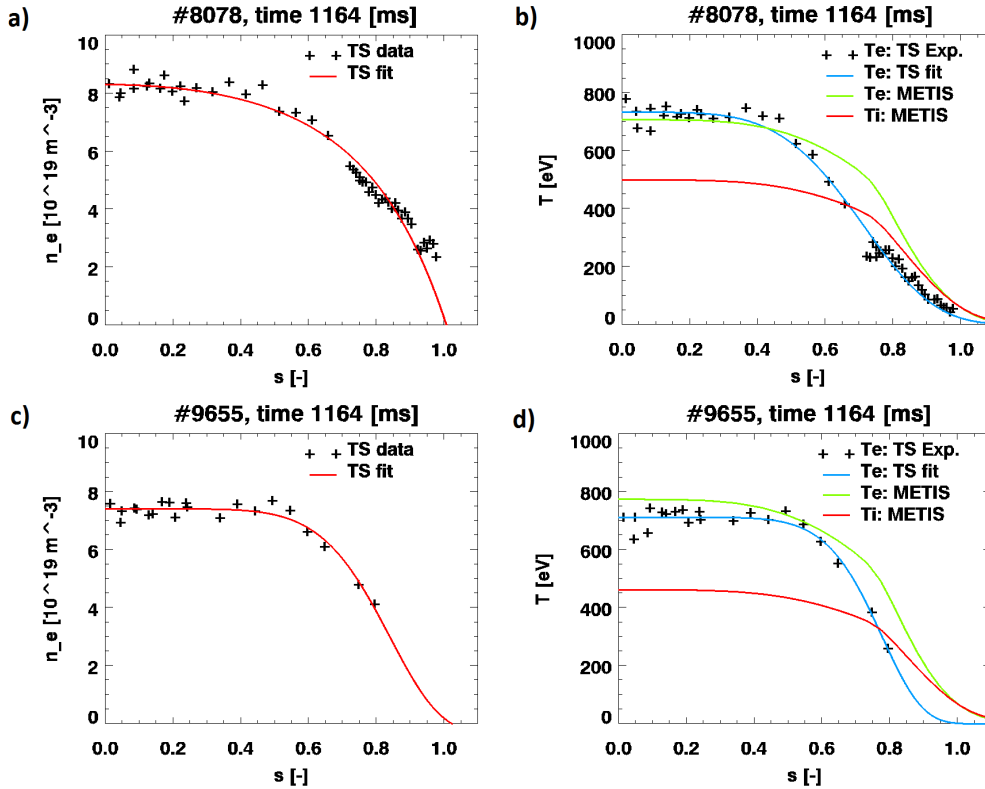
## 4.2. Modelled plasma response



**Figure 7.** Plasma density and temperature profiles measured by TS and modelled by METIS. a) $n_e$ profile of discharge #8078. b) $T_e$ of discharge #8078 as measured by TS diagnostics, in comparison to $T_e$ and $T_i$ provided by METIS simulation. c) $n_e$ profile of discharge #9655 by TS diagnostics. d) $T_e$ of discharge #9655 by TS and compared to $T_e$ and $T_i$ provided by METIS simulation.

In order to model the effect of plasma screening on $|b_{mn}^1|$ spectrum, MARS-F needs radial profiles of electron density $n_e$, electron and ion teperatures $T_e$ and $T_i$ and of toroidal plasma flow. On the COMPASS tokamak, the $n_e$ and $T_e$ profiles are provided by High-Resolution Thomson Scattering (HRTS, or TS in short) system [23, 24, 25], of spatial resolution up to 3 mm at the edge plasma, with frequency of 60 Hz - see Fig. 7 for both studied discharges. The direct measurement of $T_i$ profile is not available presently, however, it is possible to obtain the profiles of $T_e$ and $T_i$ from the METIS code simulations [26]. By overplotting all the obtained temperature profiles in Fig. 7b) and d), one can see that there is a good agreement between the results by METIS and TS. Therefore, the $T_e$ and $T_i$ profiles by METIS are used as the input for MARS-F in this paper.
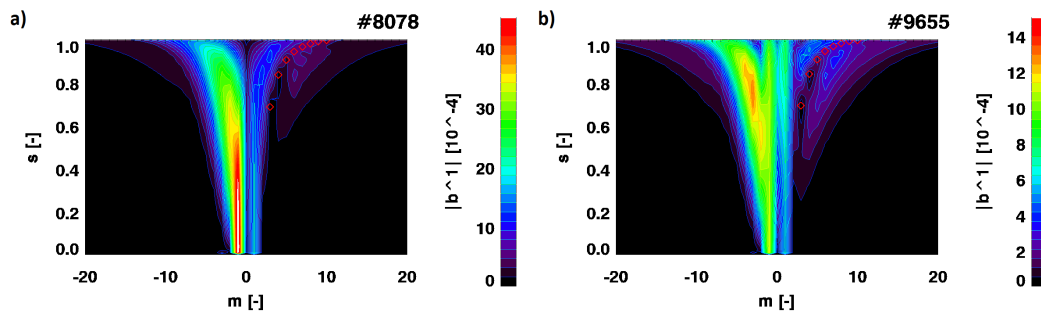
**Figure 8.** Spectrograms of the total (including plasma response) $n = 2$ RMP field $|b^1_{mn}|$, calculated by MARS-F code. a) On+off-midplane configuration of discharge #8078. b) Off-midplane configuration of discharge #9655. Red symbols represent positions where condition $q = m/n$ is fulfilled.

A sound approximation was made to equal the profile shape of toroidal plasma flow to that of $T_i$, since the measurement of this quantity is not available presently either. The magnitude of plasma toroidal rotation frequency $f_\phi$ was then obtained from the magnetic measurements of rotating MHD structures in plasma. A frequency of magnetic island rotation $f_{\mathrm{MHD}}$ is related to $f_\phi$ by relation [27]:

$$n f_\phi \approx f_{\mathrm{MHD}} - \frac{m}{2\pi r} \frac{1}{n_e q_e B_\phi} \frac{\mathrm{d}p_e}{\mathrm{d}r}, \tag{5}$$

with $q_e$ representing the electron charge and $p_e$ the electron pressure (obtained by TS). By this relation, the toroidal flow frequency on the $m/n = 3/1$ resonant position (i.e. the location of observed island) was determined, enabling the extrapolation for the other positions using the assumed profile shape. The central rotation frequency for discharge #8078 was evaluated to be $f_\phi(0) = 17.96$ kHz, while for discharge #9655 $f_\phi(0) = 15.11$ kHz. Given the number of approximations made here, the robustness of the modelled plasma response with respect to plasma rotation (specifically by increase in rotation via neglecting the diamagnetic drift term) is investigated in Section 4.3.

The resulting $|b^1_{mn}|$ spectrograms, with the plasma response included, are shown in Fig. 8a) and b) for the on+off-midplane configuration and the off-midplane configuration, respectively. By comparison to the spectra of the original vacuum perturbations in Fig. 6, it can be seen that the screening effect of plasma is strong in both studied discharges. The pitch-aligned components of the perturbation field, whose positions are depicted by red symbols are on low magnitudes. However, the significant shift of field spectrum from resonant components of positive $m$ to the negative $m$ values of non-resonant components was not trivially expected. The described distortion of the RMP spectrum associated with the $B^{resp}_{n2}$ quantity is further discussed in Section 5.

Additional insight into the nature of RMP screening on COMPASS is provided by Fig. 9. Here, the magnitudes of pitch-aligned components of $|b^1_{mn}|$ across the $q = m/n$ resonant surfaces are shown - the original perturbation versus the perturbation with plasma response included. First, comparing the on+off-midplane configuration in Fig. 9a) to the off-midplane configuration in fig. 9b) once again shows, that the magnitude
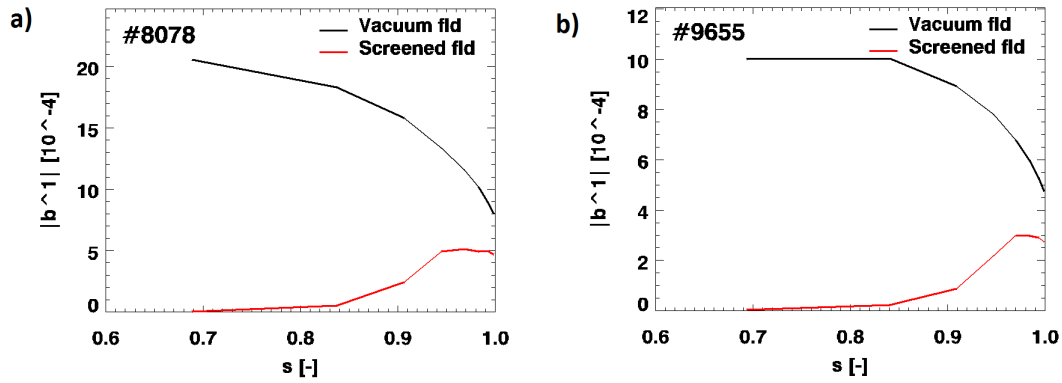
**Figure 9.** Amplitudes of the pitch-aligned components of RMP of the original vacuum perturbation (black) and of the plasma-screened perturbation (red). a) On+off-midplane configuration of discharge #8078. b) Off-midplane configuration of discharge #9655.

of generated resonant field is significantly lower in the absence of large midplane coil row. From the viewpoint of the RMP field penetration into the plasma, both plots show shallow penetration, which takes place at approximately the same depth, regardless of the RMP configuration. Simulations with the quasi-linear MARS-Q code [16] are planned within the scope of future work, where the modelled penetration of the RMP is expected to reach deeper into the plasma [29].
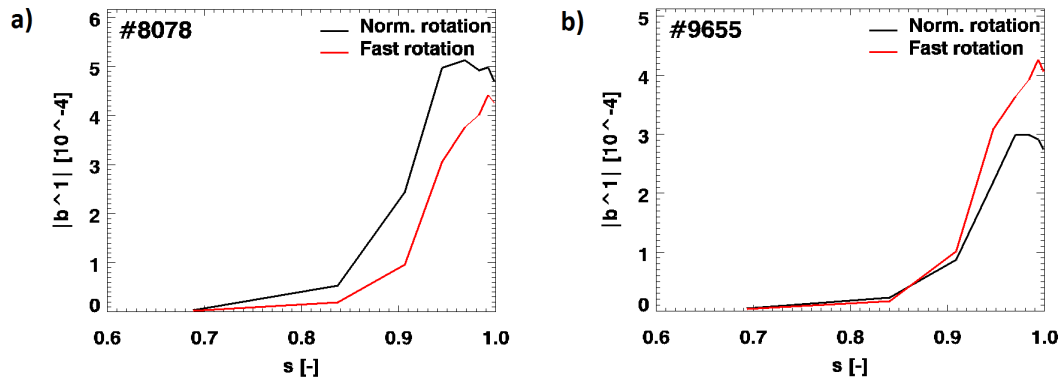
### 4.3. Effect of higher plasma rotation



**Figure 10.** Amplitudes of the pitch-aligned components of the screened RMP field, with original $f_\phi$ (black) and with $f_\phi$ with diamagnetic drift term neglected (red). a) On+off-midplane configuration of discharge #8078. b) Off-midplane configuration of discharge #9655.

By neglecting the diamagnetic drift term in Eq. (5), the central toroidal rotation (assuming the profile shape equivalent to $T_i$ in Fig. 7), shifts from $f_{\phi 1} = 17.96$ kHz to $f_{\phi 2} = 51.48$ kHz for discharge #8078, and from $f_{\phi 1} = 15.11$ kHz to $f_{\phi 2} = 43.46$ kHz for discharge #9655. By using such a high rotation values for input of the simulation,

it is possible to investigate the robustness of the calculation with respect to the effect of possible uncertainties in $f_\phi$.

The results of the simulations are shown in Fig. 10 on the pitch-aligned components of $|b_{mn}^1|$, also showing the results of the simulations using the original rotation for reference. It can be seen that the penetration depth of RMP into plasma did not significantly change in both the amplitude as well as the radial profile of the resonant $|b_{mn}^1|$ quantity. Taken into consideration the large difference between the respective $f_\phi$ used in the simulations, it is concluded that the results are not significantly sensitive to the possible experimental uncertainties in determination of $f_\phi$ quantity.

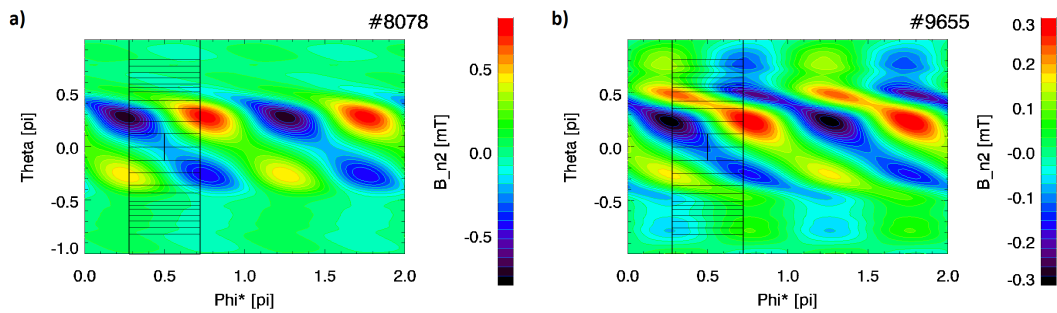## 5. Comparison of the simulated $B_{n2}^{Resp}$ to the measurements



**Figure 11.** $\theta - \phi$ profile of $B_{n2}^{resp}$ as calculated by MARS-F. a) On+off-midplane configuration of discharge #8078. b) Off-midplane configuration of discharge #9655. The black lines represent positions of the saddle loops, over which the averaging for Fig. 12 took place. Note that the depicted saddle loop scheme is simplified for clarity.
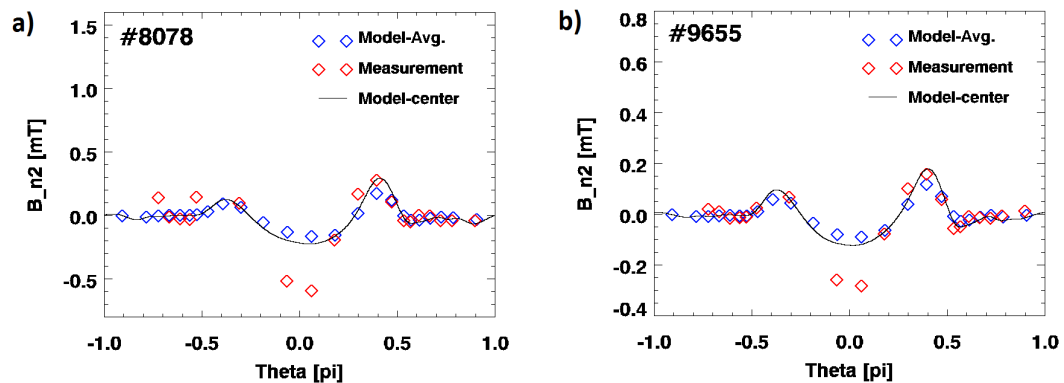


**Figure 12.** $\theta$ profile of $B_{n2}^{resp}$ field, both measured by saddle loops (red symbols) and modelled by MARS-F. Simulated quantity is shown for both the $\phi$ position in the middle of saddle loops (black line), as well as for the modelled field averaged across surface spanned by saddle loops (blue symbols). a) On+off-midplane configuration of discharge#8078. b) Off-midplane configuration of discharge #9655.

To compare the MARS-F simulated plasma response field to the experimentally determined quantity of $B_{n2}^{Resp}$ from Section 3, a more appropriate quantity than the

$|b^1_{mn}|$ spectrum is necessary. Specifically, the component of the total (with respect to $m$) magnetic field of $n = 2$ periodicity, radially located on the tokamak chamber and of normal direction to this surface is used. The magnetic field component representing the plasma response is obtained using Eq. (2), with $B^{Vac}_{n2}$ representing the vacuum perturbation field from Section 4.1, and $B^{Tot}_{n2}$ representing the screened perturbation field from Section 4.2.

The resulted modelled $B^{Resp}_{n2}$ $\theta - \phi$ profile is depicted in Fig. 11a) and b), for on+off-midplane and off-midplane RMP configuration, respectively. Comparison of these profiles to the measurements in Fig. 5, shows that the used model reproduces both the helical character of the $B^{Resp}_{n2}$, as well as its poloidal localization in the $-\pi/2 < \theta < \pi/2$ range. It should be noted however, that the measured response in Fig. 5 and the simulated response in Fig. 11 are not entirely the same quantity as the former is averaged across the whole surface of a saddle loop. Therefore, the known $\theta - \phi$ dimensions of the detection saddle loops are used to average the modelled local $B^{Resp}_{n2}$ field across the loop surfaces (see Fig. 11). The appropriate toroidal positioning of the loop mesh was validated by checking the agreement between the measured $B^{Vac}_{n2}$ and the modelled one upon averaging. It should be also noted that, while for the simplicity the loop system in Fig. 11 has no port-avoiding turns (e.g. seen in Fig. 2), they are in fact implemented into the averaging procedure.

The model-averaged and the measured $B^{Resp}_{n2}$ are compared in Fig. 12a) and b), for on+off-midplane configuration and off-midplane configuration, respectively, with the black line representing the local modelled $B^{Resp}_{n2}$ on the toroidal position $\phi^* = 0.5\pi$. The similarity of the averaged field to this line illustrates that the loop averaging is from the most part symmetric with respect to this position. More importantly, Fig. 12 shows a good agreement between the linear MARS-F model and the measurements for the plasma RMP response to the both tested RMP field configurations across the most of the poloidal angle $\theta$. Linking this to the simulated strong plasma screening effects reported in Section 4.2, together with the observations of spatial anti-phase of $B^{Resp}_{n2}$ to $B^{Vac}_{n2}$, it confirms that the measured $B^{Resp}_{n2}$ is indeed expected to be an order below the original perturbation.

There is, however, a notable discrepancy between the simulated and measured $B^{Resp}_{n2}$ in the LFS area. Specifically, the measured LFS plasma response field is dominant over that corresponding to the locations of the bottom and the top rows of the RMP coils ($\theta \approx 0.4\pi$) by approximately a factor of 2. This is not observed in the simulated results and will be subject to investigation in the future work, e.g. by using quasi-linear modelling with MARS-Q to take into account moment transport and its effect on plasma screening [29], or by using more relevant profiles of toroidal plasma flow, obtained from the CXRS measurements [30].

## 6. Summary

Two configurations of the $n = 2$ RMP field on the COMPASS tokamak were introduced. They differ by presence or absence of the large RMP coils on the midplane, in addition to the standard bottom and top row coils of even parity. The RMP field was analysed from two different perspectives:

- By magnetic measurements using the extensive set of 104 saddle loops covering the whole tokamak vessel.
- By linear MHD simulations using the MARS-F code, based on the measurements and simulations of the plasma equilibrium and profiles.

In the experiment, it was observed, that for both of the studied RMP configurations, the plasma response field of $B_{n2}^{Resp}$ is close to being in anti-phase to the original perturbation of $B_{n2}^{Vac}$ as well as being approximately one order of magnitude below the $B_{n2}^{Vac}$. The shape of the plasma response field profile along $\theta$ was reported to be invariant to the inclusion of the large RMP coils on the midplane. The ratio between the $B_{n2}^{Resp}$ magnitudes on the poloidal positions of $\theta \approx 0.4\pi$, where the top and the bottom row of the RMP coils are located, and the midplane magnitude, remains $\approx 0.5$ across the studied RMP configurations. The large midplane RMP coils, however, have a significant effect on the magnitude of RMP field as a whole.

By modelling the RMP configurations with the MARS-F code, it was seen that there is a good resonance between the original, non-screened RMP and the chosen plasma equilibria. Similarly to the experimental observations, the midplane RMP coils row was seen to have significant effect on the magnitude of the perturbation as a whole. Simulations of the plasma response have revealed a strong screening effect of the plasma on the RMP spectra, consistent with the experimentally observed phase shift between $B_{n2}^{Resp}$ and $B_{n2}^{Vac}$. Also, both the experiment and the model show that $B_{n2}^{Resp}$ is of helical character in $\theta - \phi$ plane. According to the linear model simulations, the penetration of the RMP into the COMPASS plasma is shallow.

A good agreement between the $B_{n2}^{Resp}$ from the experiment and the model is reported across the most of the $\theta$ profile, with exception of the discrepancy on the LFS. The reason for this is currently under investigation. This may be associated to the physics not taken into account by the linear model, or with the variation of the toroidal plasma flow profiles. Future endeavours in this specific area will thus include simulations by the quasilinear MHD code MARS-Q, more accurate measurements of the $T_i$ and $f_\phi$ profiles by using CXRS, and attempts to direct measurements of the screening currents.

### Acknowledgments

[1] R. Pánek, J. Adámek, M. Aftanas, P. Bílková, P. Bohm, F. Brochard, P. Cahyna, J. Cavalier, R. Dejarnac, M. Dimitrova, O. Grover, J. Harrison, P. Háček, J. Havlíček, A. Havránek, J. Horáček, M. Hron, M. Imríšek, F. Janky, A. Kirk, M. Komm, K. Kovařík, J. Krbec, L. Kripner, T. Markovič, K. Mitošinková, J. Mlynář, D. Naydenkova, M. Peterka, J. Seidl, J. Stockel, E. Štefániková, M. Tomeš, J. Urban, P. Vondráček, M. Varavin, J. Varju, V. Weinzettl, J. Zajac, and the COMPASS team. Status of the COMPASS tokamak and characterization of the first H-mode. *Plasma Physics and Controlled Fusion*, 58(1):014015, 2016.

[2] Y. Q. Liu, A. Bondeson, C. M. Fransson, B. Lennartson, and C. Breitholtz. Feedback stabilization of nonaxisymmetric resistive wall modes in tokamaks. I. electromagnetic model. *Physics of Plasmas*, 7(9), 2000.

[3] A. Loarte, G. Saibene, R. Sartori, D. Campbell, M. Becoulet, L. Horton, T. Eich, A. Herrmann, G. Matthews, N. Asakura, A. Chankin, A. Leonard, G. Porter, G. Federici, G. Janeschitz, M. Shimada, and M. Sugihara. Characteristics of type I ELM energy and particle losses in existing devices and their extrapolation to ITER. *Plasma Physics and Controlled Fusion*, 45(9):1549, 2003.

[4] T. E. Evans. ELM mitigation techniques. *Journal of Nuclear Materials*, 438, Supplement:S11 – S18, 2013. Proceedings of the 20th International Conference on Plasma-Surface Interactions in Controlled Fusion Devices.

[5] P. T. Lang, G. D. Conway, T. Eich, L. Fattorini, O. Gruber, S. Gunter, L.D. Horton, S. Kalvin, A. Kallenbach, M. Kaufmann, G. Kocsis, A. Lorenz, M. E. Manso, M. Maraschek, V. Mertens, J. Neuhauser, I. Nunes, W. Schneider, W. Suttrop, H. Urano, and the ASDEX Upgrade Team. ELM pace making and mitigation by pellet injection in ASDEX upgrade. *Nuclear Fusion*, 44(5):665, 2004.

[6] A. W. Degeling, Y. R. Martin, J. B. Lister, L. Villard, V. N. Dokouka, V. E. Lukash, and R. R. Khayrutdinov. Magnetic triggering of ELMs in TCV. *Plasma Physics and Controlled Fusion*, 45(9):1637, 2003.

[7] T. E. Evans, R. A. Moyer, P. R. Thomas, J. G. Watkins, T. H. Osborne, J. A. Boedo, E. J. Doyle, M. E. Fenstermacher, K. H. Finken, R. J. Groebner, M. Groth, J. H. Harris, R. J. La Haye, C. J. Lasnier, S. Masuzaki, N. Ohyabu, D. G. Pretty, T. L. Rhodes, H. Reimerdes, D. L. Rudakov, M. J. Schaffer, G. Wang, and L. Zeng. Suppression of large edge-localized modes in high-confinement DIII-D plasmas with a stochastic magnetic boundary. *Phys. Rev. Lett.*, 92:235003, Jun 2004.

[8] Y. Liang, H. R. Koslowski, P. R. Thomas, E. Nardon, B. Alper, P. Andrew, Y. Andrew, G. Arnoux, Y. Baranov, M. Bécoulet, M. Beurskens, T. Biewer, M. Bigi, K. Crombe, E. De La Luna, P. de Vries, W. Fundamenski, S. Gerasimov, C. Giroud, M. P. Gryaznevich, N. Hawkes, S. Hotchin, D. Howell, S. Jachmich, V. Kiptily, L. Moreira, V. Parail, S. D. Pinches, E. Rachlew, and O. Zimmermann. Active control of Type-I Edge-Localized Modes with $n = 1$ perturbation fields in the JET tokamak. *Phys. Rev. Lett.*, 98:265004, Jun 2007.

[9] T. E. Evans, M. E. Fenstermacher, R. A. Moyer, T. H. Osborne, J. G. Watkins, P. Gohil, I. Joseph, M. J. Schaffer, L. R. Baylor, M. Bécoulet, J. A. Boedo, K. H. Burrell, J. S. deGrassie, K. H. Finken, T. Jernigan, M. W. Jakubowski, C. J. Lasnier, M. Lehnen, A. W. Leonard, J. Lonnroth, E. Nardon, V. Parail, O. Schmitz, B. Unterberg, and W. P. West. RMP ELM suppression in DIII-D plasmas with ITER similar shapes and collisionalities. *Nuclear Fusion*, 48(2):024002, 2008.

[10] W. Suttrop, T. Eich, J. C. Fuchs, S. Gunter, A. Janzer, A. Herrmann, A. Kallenbach, P. T. Lang, T. Lunt, M. Maraschek, R. M. McDermott, A. Mlynek, T. Putterich, M. Rott, T. Vierle, E. Wolfrum, Q. Yu, I. Zammuto, and H. Zohm. First observation of edge localized modes mitigation with resonant and nonresonant magnetic perturbations in ASDEX Upgrade. *Phys. Rev. Lett.*, 106:225004, Jun 2011.

[11] A. Kirk, Y. Q. Liu, E. Nardon, P. Tamain, P. Cahyna, I. Chapman, P. Denner, H. Meyer, S. Mordijck, D. Temple, and the MAST team. Magnetic perturbation experiments on MAST L-

and H-mode plasmas using internal coils. *Plasma Physics and Controlled Fusion*, 53(6):065011, 2011.

[12] A. D. Turnbull. Plasma response models for non-axisymmetric perturbations. *Nuclear Fusion*, 52(5):054016, 2012.

[13] P. Denner, Y. Liang, Y. Yang, M. Rack, L. Zeng, J. Pearson, Y. Xu, and the TEXTOR Team. Local measurements of screening currents driven by applied RMPs on TEXTOR. *Nuclear Fusion*, 54(6):064003, 2014.

[14] P. Cahyna, R. Pánek, V. Fuchs, L. Krlín, M. Bécoulet, G. Huysmans, and E. Nardon. The optimization of resonant magnetic perturbation spectra for the COMPASS tokamak. *Nuclear Fusion*, 49(5):055024, 2009.

[15] J. Havlicek, R. Hauptmann, O. Peroutka, M. Tadros, M. Hron, F. Janky, P. Vondracek, P. Cahyna, O. Mikulín, D. Šesták, P. Junek, and R. Pánek. Power supplies for plasma column control in the COMPASS tokamak. *Fusion Engineering and Design*, 88(910):1640 – 1645, 2013. Proceedings of the 27th Symposium On Fusion Technology (SOFT-27); Liege, Belgium, September 24-28, 2012.

[16] Y. Q. Liu, A. Kirk, and Y. Sun. Toroidal modeling of penetration of the resonant magnetic perturbation field. *Physics of Plasmas*, 20(4):–, 2013.

[17] L.L. Lao, H. St. John, R.D. Stambaugh, A.G. Kellman, and W. Pfeiffer. Reconstruction of current profile parameters and plasma shapes in tokamaks. *Nuclear Fusion*, 25(11):1611, 1985.

[18] L. C. Appel, G. T. A. Huysmans, L. L. Lao, P. J. McCarthy, D. G. Muir, E. R. Solano, J. Storrs, D. Taylor, W. Zwingmann, et al. A unified approach to equilibrium reconstruction. In *Proceedings-33rd EPS conference on Controlled Fusion and Plasma Physics, pp. P–2.160*, 2006.

[19] H. Lutjens, A. Bondeson, and O. Sauter. The CHEASE code for toroidal MHD equilibria. *Computer Physics Communications*, 97(3):219 – 260, 1996.

[20] D. A. Ryan, Y. Q. Liu, A. Kirk, W. Suttrop, B. Dudson, M. Dunne, R. Fischer, J. C. Fuchs, M. Garcia-Munoz, B. Kurzan, P. Piovesan, M. Reinke, M. Willensdorfer, the ASDEX-Upgrade team, and the EUROfusion MST1 team. Toroidal modelling of resonant magnetic perturbations response in ASDEX-Upgrade: coupling between field pitch aligned response and kink amplification. *Plasma Physics and Controlled Fusion*, 57(9):095008, 2015.

[21] E. Nardon, M. Bécoulet, G. Huysmans, O. Czarny, P. R. Thomas, M. Lipa, R. A. Moyer, T. E. Evans, G. Federici, Y. Gribov, A. Polevoi, G. Saibene, A. Portone, and A. Loarte. Edge localized modes control by resonant magnetic perturbations. *Journal of Nuclear Materials*, 363365:1071 – 1075, 2007. Plasma-Surface Interactions-17.

[22] E. Nardon. *Edge localized modes control by resonant magnetic perturbations*. PhD thesis, Ecole Polytechnique, 2007.

[23] Design of new thomson scattering diagnostic system on COMPASS tokamak. *Nuclear Instruments and Methods in Physics Research Section A: Accelerators, Spectrometers, Detectors and Associated Equipment*, 623(2):656 – 659, 2010. 1rs International Conference on Frontiers in Diagnostics Technologies.

[24] P. Bílková, R. Melich, M. Aftanas, P. Bohm, D. Sestak, D. Jares, V. Weinzettl, J. Stockel, M. Hron, R. Pánek, R. Scannell, and M. J. Walsh. Progress of development of thomson scattering diagnostic system on COMPASS. *Review of Scientific Instruments*, 81(10), 2010.

[25] P. Bohm, M. Aftanas, P. Bilkova, E. Stefanikova, O. Mikulin, R. Melich, F. Janky, J. Havlicek, D. Sestak, V. Weinzettl, J. Stockel, M. Hron, R. Panek, R. Scannell, L. Frassinetti, A. Fassina, G. Naylor, and M. J. Walsh. Edge thomson scattering diagnostic on COMPASS tokamak: Installation, calibration, operation, improvements. *Review of Scientific Instruments*, 85(11), 2014.

[26] J. F. Artaud, V. Basiuk, F. Imbeaux, M. Schneider, J. Garcia, G. Giruzzi, P. Huynh, T. Aniel, F. Albajar, J. M. Ané, A. Bécoulet, C. Bourdelle, A. Casati, L. Colas, J. Decker, R. Dumont, L. G. Eriksson, X. Garbet, R. Guirlet, P. Hertout, G. T. Hoang, W. Houlberg, G. Huysmans, E. Joffrin, S.H. Kim, F. Kochl, J. Lister, X. Litaudon, P. Maget, R. Masset, B. Pégourié,

Y. Peysson, P. Thomas, E. Tsitrone, and F. Turco. The CRONOS suite of codes for integrated tokamak modelling. *Nuclear Fusion*, 50(4):043001, 2010.

[27] M. De Bock. *Understanding and controllig plasma rotation in tokamaks.* PhD thesis, Technische Universiteit Eindhoven, 2007.

[28] Y. Q. Liu, A. Kirk, Y. Gribov, M. P. Gryaznevich, T. C. Hender, and E. Nardon. Modelling of plasma response to resonant magnetic perturbation fields in MAST and ITER. *Nuclear Fusion*, 51(8):083002, 2011.

[29] Y. Q. Liu, A. Kirk, Y. Sun, P. Cahyna, I. T. Chapman, P. Denner, G. Fishpool, A. M. Garofalo, J. R. Harrison, E. Nardon, and the MAST team. Toroidal modeling of plasma response and resonant magnetic perturbation field penetration. *Plasma Physics and Controlled Fusion*, 54(12):124013, 2012.

[30] V. Weinzettl, G. Shukla, J. Ghosh, R. Melich, R. Panek, M. Tomes, M. Imrisek, D. Naydenkova, J. Varju, T. Pereira, R. Gomes, I. Abramovic, R. Jaspers, M. Pisarik, T. Odstrcil, and G. Van Oost. High-resolution spectroscopy diagnostics for measuring impurity ion temperature and velocity on the COMPASS tokamak. *Fusion Engineering and Design*, 9697:1006 – 1011, 2015. Proceedings of the 28th Symposium On Fusion Technology (SOFT-28).